Journal of Applied Geophysics 150 (2018) 40–51

Contents lists available at ScienceDirect

Journal of Applied Geophysics

journal homepage: www.elsevier.com/locate/jappgeo

Combined DC resistivity and induced polarization (DC-IP) for mapping the internal composition of a mine waste rock pile in Nova Scotia, Canada

Christopher Power [a,*], Panagiotis Tsourlos [b], Murugan Ramasamy [a], Aristeidis Nivorlis [c], Martin Mkandawire [a]

[a] Verschuren Centre, Cape Breton University, Sydney, Nova Scotia, Canada
[b] Department of Geophysics, Aristotle University of Thessaloniki, Thessaloniki, Greece
[c] Engineering Geology Department, Lund University, Lund, Sweden

ARTICLE INFO

Article history:
Received 22 September 2017
Received in revised form 10 January 2018
Accepted 12 January 2018
Available online 16 January 2018

Keywords:
Geoelectrical characterization
Electrical resistivity
Normalized chargeability
Acid mine drainage
Groundwater contamination
Sulfide minerals

ABSTRACT

Mine waste rock piles (WRPs) can contain sulfidic minerals whose interaction with oxygen and water can generate acid mine drainage (AMD). Thus, WRPs can be a long-term source of environmental pollution. Since the generation of AMD and its release into the environment is dependent on the net volume and bulk composition of waste rock, effective characterization of WRPs is necessary for successful remedial design and monitoring. In this study, a combined DC resistivity and induced polarization (DC-IP) approach was employed to characterize an AMD-generating WRP in the Sydney Coalfield, Nova Scotia, Canada. Two-dimensional (2D) DC-IP imaging with 6 survey lines was performed to capture the full WRP landform. 2D DC results indicated a highly heterogeneous and moderately conductive waste rock underlain by a resistive bedrock containing numerous fractures. 2D IP (chargeability) results identified several highly-chargeable regions within the waste, with normalized chargeability delineating regions specific to waste mineralogy only. Three-dimensional (3D) DC-IP imaging, using 17 parallel lines on the plateau of the pile, was then used to focus on the composition of the waste rock. The full 3D inverted DC-IP distributions were used to identify coincident and continuous zones (isosurfaces) of low resistivity (<30 Ω-m) and high normalized chargeability (>0.4 mS/m) that were inferred as generated AMD (leachate) and stored AMD (sulfides), respectively. Integrated geological, hydrogeological and geochemical data increased confidence in the geoelectrical interpretations. Knowledge on the location of potentially more reactive waste material is extremely valuable for improved long-term AMD monitoring at the WRP.

1. Introduction

Mine waste rock piles (WRPs) are the product of the on-site disposal of waste rock produced during mining activities. The waste rock is typically characterized by non-economic minerals with high metal and metalloid contents. WRPs can contain significant quantities of sulfidic minerals such as pyrite and pyrrhotite, and interaction of these reactive minerals with oxygen and water can trigger a complex sequence of oxidation–reduction reactions that produce an acidified leachate. This process is known as acid mine drainage (AMD) (Nordstrom et al., 2015). The leachate is characterized by low pH and high sulfate and can further dissolve and become enriched by heavy metals and other toxic elements (INAP (The International Network for Acid Prevention), 2014). AMD can emanate from WRPs for extended periods and be a long-term source for severe environmental pollution (e.g., Amos et al., 2015; Power et al., 2017a).

The generation of AMD within WRPs is strongly dependent on the volume, structure and composition of the waste rock. The waste rock grain size can vary from clayey and silty particles to meter-sized blocks, and this widely spread gradation can create significant heterogeneity in the pile, including material properties and moisture distribution (e.g., Anterrieu et al., 2010). For example, fine-grained materials exhibit larger surface area, a higher water retention capacity and a lower permeability than coarse-grained materials. Therefore, assessing the heterogeneity and internal composition of WRPs, particularly the distribution of any reactive minerals, is necessary to assist and improve remedial design and long-term performance.

Characterization of the internal WRP structure, which can contain millions of tonnes of waste rock, and cover several hectares over a thickness of tens of meters, is challenging. Conventional methods, including boreholes and test pits, are expensive and suffer from low sampling density, providing limited spatial information in such highly heterogeneous material. Geoelectrical methods, such as DC resistivity, induced polarization (IP), electromagnetics (EM) and ground penetrating radar (GPR), can provide large-scale continuous mapping of physical properties and their variations. Measured properties such as electrical resistivity, chargeability and dielectric constant are known to be

* Corresponding author.
E-mail addresses: chris_power@cbu.ca (C. Power), tsourlos@geo.auth.gr (P. Tsourlos), murugan_ramasamy@cbu.ca (M. Ramasamy), aristeidis.nivorlis@tg.lth.se (A. Nivorlis), martin_mkandawire@cbu.ca (M. Mkandawire).

https://doi.org/10.1016/j.jappgeo.2018.01.009
0926-9851/

correlated to several hydrogeological and geochemical parameters (e.g., porosity, degree of saturation, water chemistry, mineralogical composition). Geoelectrical methods are employed in a wide range of hydrogeological and environmental investigations (e.g., Binley et al., 2015; Loke et al., 2013; Revil et al., 2012), including geology (e.g., Chambers et al., 2006), groundwater-surface water interactions (e.g., Slater et al., 2010), salt-water intrusion (e.g., de Franco et al., 2009), groundwater contamination (e.g., Power et al., 2013), landfill leachate (e.g., Aristodemou and Thomas-Betts, 2000) and moisture content (e.g., Zhou et al., 2001).

Despite this potential, only a handful of published studies exist that have applied geoelectrical methods to characterize WRPs at active or abandoned mine sites. Most studies have applied geoelectrical methods to delineate AMD plumes emanating from mine site landforms such as tailings impoundments. While some studies have successfully applied a single method to map AMD, such as DC resistivity (e.g., Rucker et al., 2009) and EM induction (e.g., Ladwig, 1983), other studies have combined two or more geoelectrical methods (e.g., Campbell and Fitterman, 2000). DC resistivity and EM were combined in various studies to map AMD-impacted groundwater (e.g., Spindler and Olyphant, 2004), while Buselli et al. (1998) integrated DC, EM and IP to map preferential groundwater flow pathways through a tailings dam. Yuval and Oldenburg (1996) combined DC resistivity and IP (hereafter termed DC-IP) to image AMD-contaminated water migrating from a mine tailings impoundment. Distributions of electrical resistivity and chargeability were correlated to concentrations of total dissolved solids (TDS) in the tailings water and the concentration of sulfide minerals, respectively. Combined DC-IP has also been used to successfully image heterogeneous buried waste at landfills (e.g., Carlson et al., 2015; Gazoty et al., 2012), which is analogous to WRP investigations.

A large portion of the studies on geoelectrical imaging of WRPs has been conducted at the Laronde WRP in Quebec, Canada. Campos et al. (2003) and Poisson et al. (2009) evaluated the potential of DC, EM and GPR for imaging shallow structural variations and moisture distributions in the pile, with results being corroborated by hydrogeological field and laboratory studies (e.g., Fala et al., 2005). While these preliminary studies were constrained to a small test area on the pile, Anterrieu et al. (2010) expanded the geophysical investigation to characterize the main structural features of the entire WRP. Data from DC, EM and GPR surveys were complemented by hydrogeological, geochemical and geotechnical information obtained from a limited set of samples taken from trenches. Studies conducted at other WRPs include Campbell et al. (1998), who used spectral IP to identify sulfide minerals at a WRP in Colorado, USA, and van Dam et al. (2005), who employed GPR and EM to conduct a structural analysis of a WRP in New Mexico, USA. Mele et al. (2013) employed DC resistivity to characterize the Antenna WRP in Elba Island, Italy, and delineate the extent of the near-surface, highly conductive waste rock from the less-permeable, higher resistivity bedrock. While these studies relied on individual 2D images to infer the structure of WRPs, full 3D imaging is expected to more realistically resolve the complex structure and heterogeneity involved (e.g., Papadopoulos et al., 2006).

All aforementioned studies have employed DC resistivity at WRPs, either standalone, or as part of an integrated approach. Variations in measured electrical resistivity have been used to infer zones with elevated concentrations of metals and TDS, which are associated with conductive waste rock or acid leachate plumes (e.g., Mele et al., 2013; Rucker et al., 2009). Time-domain IP, which is a method that is complementary to DC resistivity, has long standing potential for mapping variations in mineralogical composition; however, very few, if any, published studies exist of its application at WRPs. The distribution of measured chargeability can be used to indicate areas of sulfide concentrations, which can complement the subsurface information inferred from DC resistivity (e.g., Yuval and Oldenburg, 1996). Furthermore, significant research and advances are being made in the DC-IP method, including data acquisition (e.g., Olsson et al., 2015) and processing (e.g., Nivorlis et al., 2017). DC-IP is now being increasingly used in hydrogeophysical studies, including groundwater contamination (e.g., Power et al., 2017b), municipal waste (e.g., Carlson et al., 2015) and CO_2 injection (e.g., Doetsch et al., 2015).

The objective of this study is to combine DC resistivity and induced polarization (DC-IP) to map the internal composition of a WRP in the Sydney Coalfield, Nova Scotia, Canada. Long 2D DC-IP survey lines were used to capture the general structure of the full WRP landform, including the waste rock and hosting bedrock. A 3D DC-IP survey was performed on the plateau of the pile to specifically focus on the internal composition of the waste rock. Integrated geological, hydrogeological and geochemical information was used to both assist and validate the geoelectrical interpretations.

2. Methodology

2.1. Site description

2.1.1. Waste rock pile

The Sydney Coalfield in Nova Scotia, Canada, is the oldest mined coal field in North America, with underground mining occurring from the early 1700s to the early 2000s at many sites throughout the coal field (Power et al., 2017a). Mining activities at the former Lingan Mine Colliery site occurred between 1970 and 1992, during which time approximately 28 million tonnes of coal were extracted from the Lingan Harbour Seam. During operation, surplus coal fines and mine waste rock from both the Lingan colliery and adjacent Phalen colliery were deposited into a WRP. After the closure of operations in 1992, the WRP contained 250,000 m^3 of waste rock, with an additional 130,000 m^3 of waste rock relocated from the adjacent Phalen Colliery and placed on top of the pile in 2008. The consolidated WRP contains 380,000 m^3 of waste rock, covering an area of 82,000 m^2. It is ~15 m high, with slopes ranging between 1% and 10% on top, and 4% and 20% on the sides. Fig. 1 presents a plan view of the site including the WRP.

In 2011, a cover system was placed over the WRP to reduce the infiltration of meteoric water into the waste rock, thereby reducing the seepage of AMD into the environment. The cover, which consists of a 0.5 m thick layer of till material, is the simplest cover system option for WRPs. Perimeter and drainage ditches were installed to help manage and divert runoff from the WRP and prevent soil cover erosion, while toe protection was installed at the base of the pile for long-term protection and stability. The water balance method, which is commonly used to estimate water infiltration through the cover system (e.g., Power et al., 2017a), were developed annually between 2012 and 2016. Although the cover system has reduced the water influx, 374 mm/year is still infiltrating through the cover and into the waste rock.

2.1.2. Geology and hydrogeology

A number of investigations were conducted at the site between 2004 and 2010 to assess and delineate the adverse impacts of the Lingan WRP on the receiving environment and assist in the remedial design. Several test pits and boreholes with monitoring well installations were completed within or around the footprint of the WRP, as indicated in Fig. 1. Soil stratigraphy was continuously logged with respect to soil type at each test pit and borehole.

During remedial activities in 2011, all monitoring wells were decommissioned. While soil properties are still valid from these locations, long-term groundwater monitoring was no longer possible. For this purpose, four internal monitoring stations (IMSs) were installed alongside the cover system and extended the full depth of the waste rock into the underlying shallow bedrock. During drilling of each IMS, soil stratigraphy was continuously logged, along with paste pH and electrical resistivity measurements. Fig. 2a presents the estimated geological cross-section A-A of the WRP, illustrating the waste rock and underlying till and bedrock units.

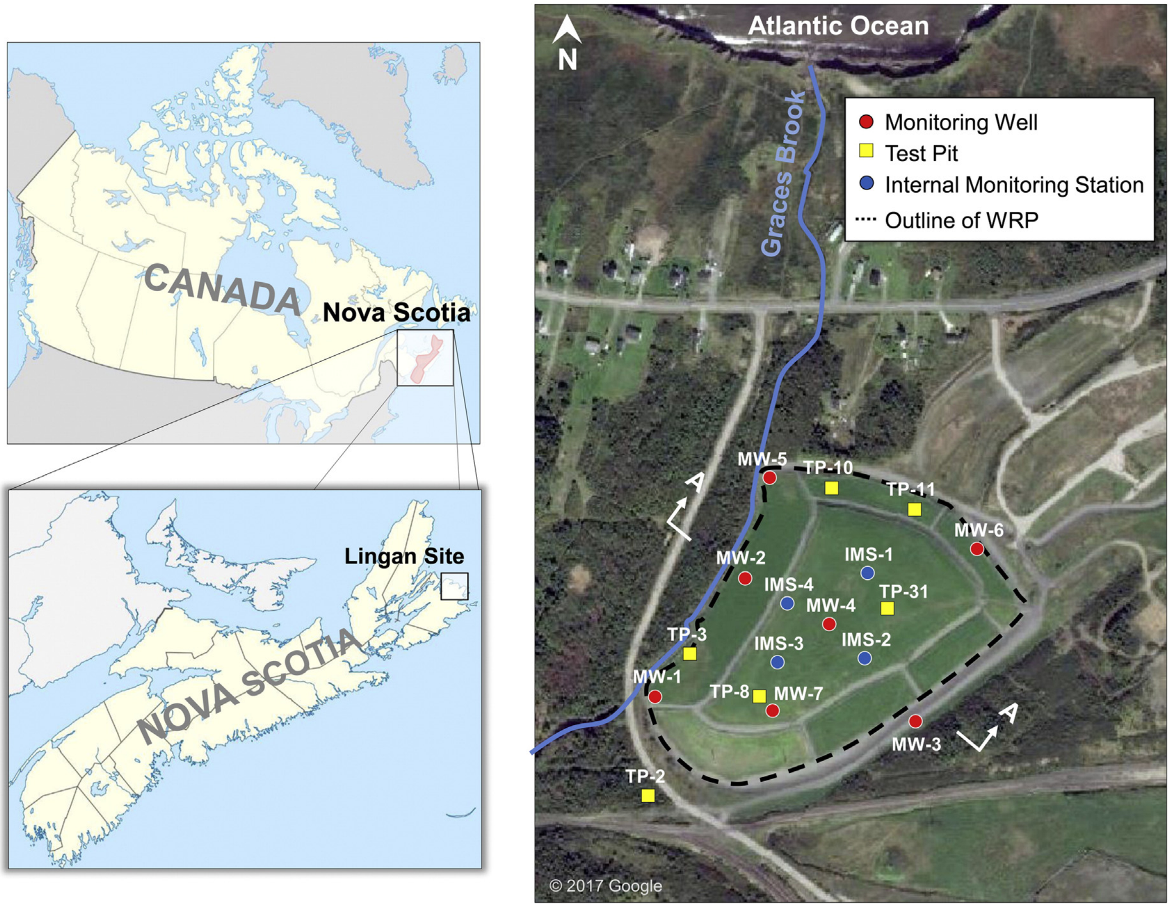

Fig. 1. The Lingan mine site location in Nova Scotia, Canada. A site plan (main) shows the Lingan WRP and surrounding area, and its close proximity to the Atlantic Ocean. The location of monitoring wells and test pits are also indicated.

The waste rock fill material consists of coarse sands, gravels, black coal and waste rock, with some timbers and construction debris encountered at some locations. The waste rock overlies a geologic unit of native till material, which consists of brown silty sand with gravel and ranges in thickness from 1 m to 4 m beneath the WRP. A bedrock unit underlies the till material that is characterized as soft, brown/grey, highly fractured and highly weathered sandstone from the Morien Group Sydney Mines Formation of the Late Carboniferous Period. Table 1 presents a summary of each geologic unit.

Groundwater levels measured at all historical monitoring wells in September 2008, and at the four IMSs in September 2015 (using the same month to obtain consistency in seasonal variation), are used to highlight the groundwater flow regime at the site. The piezometric surface and flow direction within the WRP and surrounding area are illustrated in Fig. 2b. The groundwater is predominantly flowing from southeast-to-northwest beneath the WRP. Downgradient of the WRP, shallow groundwater will likely discharge to Graces Brook, which is a stream adjacent to the western slope of the WRP flowing northwards to the Atlantic Ocean (see Fig. 1). There is no subsurface information west of Graces Brook but groundwater likely continues to flow in a northwesterly direction towards the Atlantic Ocean.

2.1.3. Acid mine drainage

Acid-base accounting (ABA), which is the most commonly used static test method for characterizing waste rock, was performed on selected waste rock samples extracted during IMS drilling in February 2011. ABA results indicated relatively low sulfide concentrations, and the WRP was classified as 'acid generating'. The presence of AMD has been observed downgradient in the receiving environment by hydrogeochemical monitoring. Groundwater flowing beneath the WRP is characterized by low pH values (5.5 to 6.5), and elevated concentrations for sulfate (up to 1100 mg/L) and metals (up to 60 mg/L for iron, 30 mg/L for manganese). Similarly, surface water sampling in Graces Brook at locations both upstream, and downstream, confirm the impacts of AMD, with surface water quality decreasing as the stream flows alongside the WRP. The primary transport pathway for AMD contamination is within the shallow groundwater, which discharges impacted groundwater to Graces Brook and/or flows west of the mine site. In both cases, the Atlantic Ocean is the ultimate receptor.

2.2. Hydrogeological and geochemical monitoring

The four IMSs were installed to permit continuous monitoring of AMD-impacted water emanating from the base of the WRP. Since installation in 2011, groundwater levels have been collected periodically along with water samples for desired chemical analysis. During the geoelectrical survey in August 2016, groundwater levels and water chemistry were measured to assist the interpretation of the geoelectrical data.

2.3. Geoelectrical surveys

2.3.1. Instrumentation

The geoelectrical field survey, combining DC resistivity and IP, was conducted in August 2016. A variety of survey lines and configurations were used to acquire the desired geoelectrical data. Fig. 3 shows the locations of each DC-IP line. UTM coordinates were recorded at key locations along every survey line (e.g., sharp change in direction or elevation) using a portable GPS station. A detailed CAD drawing of

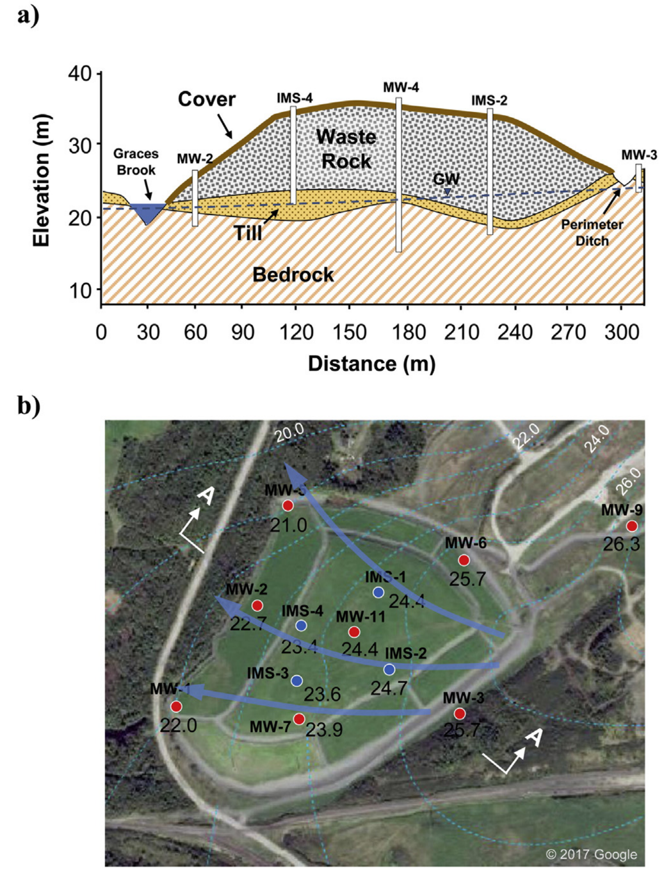

Fig. 2. (a) Estimated geological cross-section A-A through the WRP based on interpolation between sparsely located boreholes (vertical exaggeration: 5×), and (b) groundwater flow regime beneath the WRP. The blue dashed lines and blue arrows in (b) represent the piezometric surface and flow direction, respectively.

WRP topography was used to determine the elevation of every electrode along every survey line.

A Syscal Pro Switch 72 resistivity meter (Iris Instruments, France) was used to record the apparent resistivity and apparent chargeability data. Dipole-dipole and multi-gradient electrode array configurations were used to acquire two sets of resistivity data to potentially improve interpretations. Time-domain IP data (chargeability) were only acquired using the multi-gradient array configuration. Dipole-dipole generally exhibits high lateral and vertical resolution, while multi-gradient has a higher signal-to-noise (S/N) ratio (Dahlin and Zhou, 2006), which is particularly necessary for the complex heterogeneity and potentially noisy environment expected within the WRP. A time window of 0.5 s was used for resistivity measurements, while the time window for chargeability was 1 s. Strong ground coupling (<1 kΩ) was attained at all electrode locations, particularly in advance of IP measurements. Salt water was added where necessary to reduce ground resistance.

Table 1
Summary of geological units at the Lingan mine site.

Unit	Description	Thickness (m)	Mean porosity
Cover material	Till (brown silty sand)	0.5	0.38
Waste rock	Fill (gravel, sand, coal)	1–15	0.35
Till	Till (brown silty sand)	1–4	0.30
Bedrock	Sandstone (grey, highly fractured)	~25	0.15

2.3.2. Survey design

Six survey lines were deployed on the WRP to span the full spatial extent of the WRP landform. As shown in Fig. 3, lines LL01, LL02 and LL03 were orientated in a southwest-to-northeast direction, while LL04, LL05 and LL06 were orientated in a northwest-to-southeast direction, almost perpendicular to lines LL01 to LL03. The survey line layout in Fig. 3 ensured that the lines traversed adjacent to as many active IMS and former monitoring well/test pit locations as possible. For instance, LL02 traversed adjacent to IMS-1 and IMS-3, while LL05 traversed adjacent to IMS-2 and IMS-4. This known geological and hydrogeological information could be used to establish confidence in the geoelectrical data interpretations. Each survey line started at one perimeter ditch, traversing along the side slopes, drainage ditches and plateau before finishing at the opposite perimeter ditch. Lines LL05 and LL06 were extended beyond the eastern perimeter ditch to obtain subsurface electrical measurements outside the WRP footprint (Fig. 3c).

Table 2 presents a summary of survey lines LL01 to LL06. A minimum depth of investigation of 25 m was required to resolve the waste rock, till and shallow bedrock units. A minimum electrode spacing of 3 m was used with each line, with the total number of electrodes along each line ranging from 65 to 122. Since all lines apart from LL04 contained >72 electrodes (capacity of the Syscal Pro Switch 72 system), the roll-along method was used (e.g., Dahlin, 2001). For each roll-along, a maximum 36 electrodes were moved to ensure adequate overlap between each segment. DC resistivity measurements were recorded at all six survey lines, with IP chargeability measurements only recorded along the central lines: LL02 and LL05.

A 3D survey was conducted on the plateau of the WRP to obtain full 3D distributions of electrical resistivity and chargeability within the waste rock. A 2D surface grid was laid out on the plateau between all four IMSs, as shown in Fig. 3a. The grid consisted of 17 parallel survey lines, with a line separation of 5 m. A photograph of the central line LB09 is shown in Fig. 3d. Both resistivity and chargeability were measured along each line using 57 electrodes and an electrode spacing of 2.5 m. The resulting 2D surface area of 11,200 m^2 (140 m × 80 m) represents significant coverage of the pile plateau area (~25,000 m^2). The minimum depth of investigation of 20 m ensures that the complete depth of waste rock is resolved.

2.3.3. Data processing and inversion

Pre-processing of all recorded resistivity and chargeability data was performed with the recently developed BIN2IP code by Nivorlis (2017) which extended the DC resistivity data quality evaluation scheme of Kim et al. (2016) to handle both DC and time-domain IP data. The key filtering steps in this processing tool were as follows: (1) all data were filtered on the basis of their S/N ratio (i.e., measurements with low signal (high geometrical factor) and extreme apparent resistivity values were removed); (2) the mean of all measurement errors (using standard deviation of resistance) associated with every electrode was used to assess if any 'bad' electrodes existed (i.e., mispositioned or disconnected); (3) the shape of the decay curve associated with all 20 IP time windows was assessed for every measurement instead of simply using the intrinsic chargeability value. In addition to ignoring both the first 2 and last 5 time windows, measurements whose curve shape was erratic or did not decay monotonically to follow the assumed Cole-Cole model were rejected.

As an example of the decay curve shape filtering, Fig. 4 presents the IP decay curves for 3 measurements recorded at line LL02. A 'good' decay curve perfectly follows the expected gradual decay shape, while a 'moderate' decay curve contains small fluctuations. In contrast, a 'poor' decay curve fluctuates erratically, increasing and decreasing between time windows, even though it may follow a general decay. In the LL02 and LL05 chargeability datasets, <11% of the measurements were rejected due to poor decay curves, which still left at least 2200 measurements in each dataset. In all LB01 to LB17 chargeability

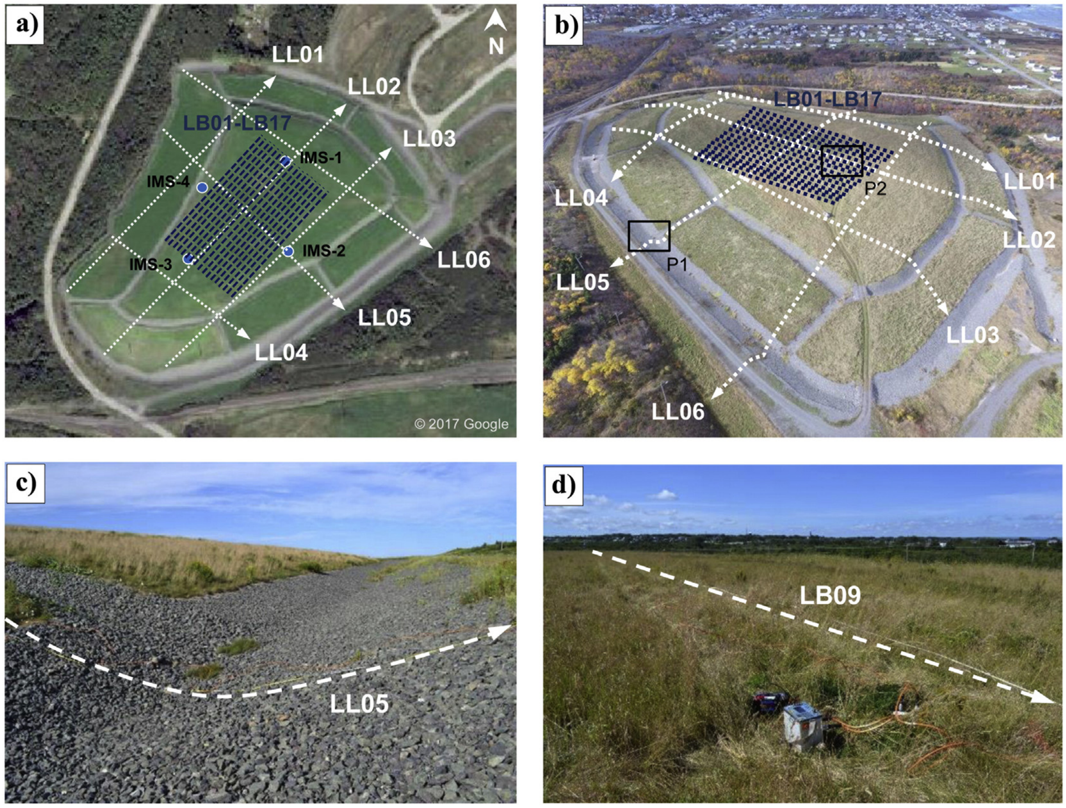

Fig. 3. Location of DC-IP survey lines indicated in (a) plan view, and (b) oblique aerial view. Photographs of (c) LL05 traversing eastern perimeter ditch (location P1), and (d) LB09 on the plateau of the WRP (location P2).

datasets, the IP decay curves were all 'good' quality with zero measurements rejected.

The recorded 2D data from the WRP landform survey lines were inverted using the DC-IP inversion program DC_2DPro (Kim, 2016), which performs 2D, iterative least-squares smoothness-constrained inversion on the recorded datasets. The elevation at each electrode was applied to include topography in the inverted sections. The 3D dataset, consisting of 17 parallel lines, was inverted with Res3DInv (Loke, 2016). All inversions were performed for a maximum of 7 iterations and had low residual RMS errors. Both dipole-dipole and multi-gradient measurements generally exhibited good data quality and similar inversion model results. However, the multi-gradient datasets required little data filtering and had lower inversion RMS errors (mean: ~3%) compared to dipole-dipole (~7%). Only multi-gradient data are shown in the results section, though dipole-dipole data were used to assist with interpretation.

The measured time-domain chargeability is a measure of the magnitude of the IP effect, and is sensitive to both the bulk conduction (electrolytic) and surface polarization (structural) properties of a material. The chargeability M can be divided by the electrical resistivity ρ to obtain a normalized chargeability M_N (i.e., $M_N = M/\rho$). Normalized chargeability has been shown to be a valuable parameter in the interpretation of field-scale IP surveys as it can help to distinguish between IP effects due to lithology and IP effects due to pore-water salinity (e.g., Slater and Lesmes, 2002; Gonzales Amaya et al., 2016). Since surface polarization processes at the mineral-fluid interface control normalized chargeability, it can be a useful parameter in detecting sulfide minerals within the WRP.

Table 2
Summary of geoelectrical survey lines conducted at the Lingan WRP.

Line	Number of electrodes	Electrode spacing (m)	Length (m)	Parameter measured[a]	Number of measurements
LL01	106	3	315	ρ	5109
LL02	122	3	363	ρ, M	6410, 2703
LL03	115	3	342	ρ	5900
LL04	65	3	192	ρ	2500
LL05	90	3	267	ρ, M	4410, 2541
LL06	106	3	315	ρ	5410
LB01 – LB17	57	2.5[b]	140	ρ, M	2850, 1845

[a] ρ (resistivity) and M (chargeability) are recorded from DC and IP modes, respectively.
[b] Interline spacing between the 17 lines was 5 m.

3. Results and discussion

3.1. Hydrogeological and geochemical data

Fig. 5 presents the depth profile recorded at each IMS, showing the general lithology and variation in electrical resistivity. The majority of

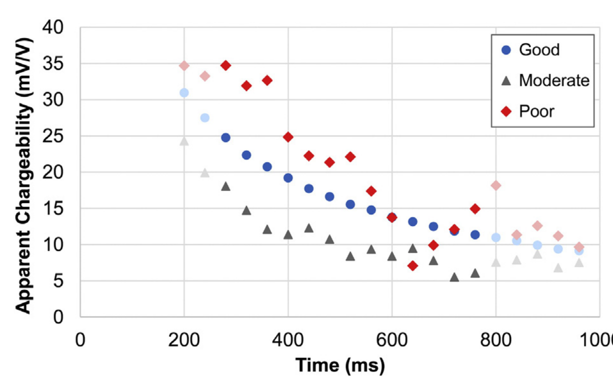

Fig. 4. Examples of IP decay curve shapes for measurements in LL02. The majority of the curves were 'good' or 'moderate' with approximately 11% of the curves considered 'poor' and therefore rejected. For all curves, the first 2, and last 5, values were neglected, as indicated by the transparent points.

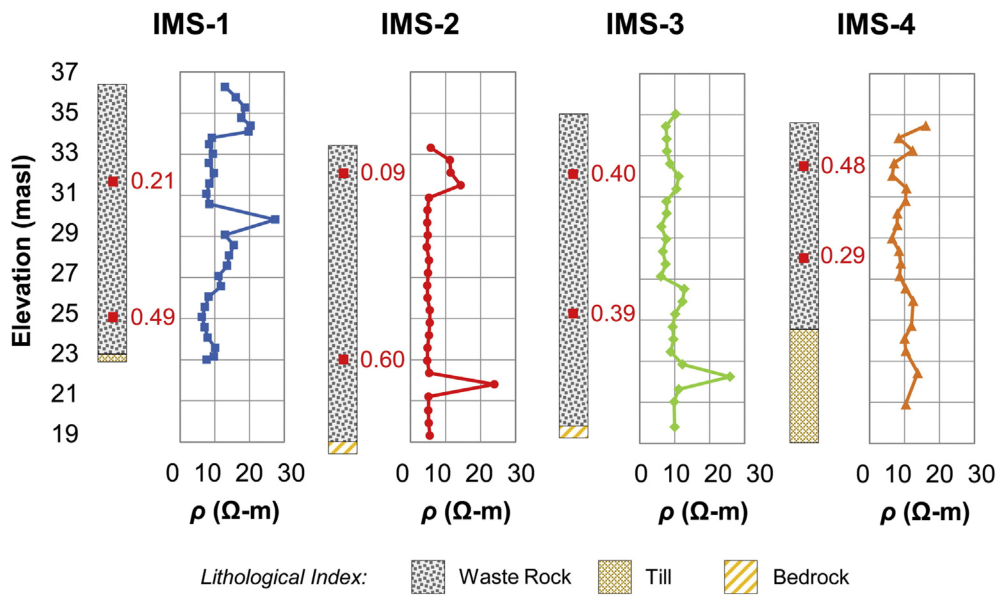

Fig. 5. Depth profile at each IMS indicating the general lithology and electrical resistivity. The location and weight percentage (wt%) of sulfide minerals determined from two waste rock samples extracted at each IMS are also indicated (red squares).

each profile contains waste rock, and while the variation within this unit is not indicated, the detailed lithology logs (not shown) confirm that the waste rock comprises a host of materials including gravel, sand, coal fines, clay and debris.

The resistivity measurements indicate that the waste material has moderately low resistivities, with mean values equal to 12.1 Ω-m, 6.8 Ω-m, 9.8 Ω-m and 9.9 Ω-m for IMS-1, IMS-2, IMS-3 and IMS-4, respectively. Aside from IMS-1, the resistivity depth profiles at the other IMSs are somewhat uniform, particularly IMS-2, which indicates a very low resistivity zone between 19 m above sea level (masl) and 31 masl. The location of waste rock samples extracted from each IMS for ABA testing are also indicated in Fig. 5 (red squares) along with the sulfide mineral concentration in weight percentage (wt%). It is evident that relatively low concentrations of sulfide exist at each location, with an average of ~0.4 wt%. However, similar concentrations have been observed at other studied WRPs (e.g., Anterrieu et al., 2010; Campbell et al., 1998).

Table 3 presents the elevation and concentration of sulfide minerals in the waste rock. The groundwater elevations and groundwater geochemistry measured at each IMS during the DC-IP survey are also shown. Integration of the water levels into the groundwater flow regime at the site demonstrated that the historical flow directions presented in Fig. 2b are unchanged (i.e., dominant flow from southeast-to-northwest).

Groundwater chemistry in Table 3 is represented by electrical conductivity (EC), total dissolved solids (TDS), total suspended solids (TSS), dissolved sulfate (SO_4), dissolved and total iron (Fe) concentrations. While EC and TDS strongly influence electrical current flow and hence the DC resistivity results, the amount of TSS in the groundwater may affect the IP response. For instance, suspended particles in the pore space and pore throat can lead to increased membrane polarization and increased chargeability during the DC-IP survey (e.g., Johansson et al., 2015). Table 3 indicates that groundwater chemistry is similar at IMS-1 and IMS-2 with high EC and high concentrations of TDS and TSS. IMS-4 exhibits similar water quality in terms of elevated TDS but has low TSS. The water chemistry at IMS-3 indicates low EC and low TDS.

3.2. 2D imaging of WRP landform

3.2.1. DC resistivity

Fig. 6 presents a fence display of the inverted electrical resistivity images for lines LL01 to LL06. The resistivity structure is coherent across all lines with good lateral and vertical continuity evident at each intersection (e.g., low resistivity body and underlying high resistivity layer at the intersection between LL03 and LL05). While the inverted images are discussed in more detail below, Fig. 6 infers three contrasting layers: (i) a thin, high resistivity near-surface layer, (ii) a lower resistivity layer

Table 3
Groundwater elevation and geochemical parameters measured during the DC-IP survey (August 2016) along with waste rock elevation and sulfide concentration measured during IMS drilling (February 2011).

Well	Groundwater							Waste rock	
	Elev (masl)	EC (μS/cm)	TDS (mg/L)	TSS (mg/L)	SO_4 (mg/L)	Fe_{DISS} (mg/L)	Fe_{TOT} (mg/L)	Elev (masl)	Sulfide (wt%)
IMS-1	24.79	1800	2800	5800	870	0.7	710	31.5	0.21
								25.1	0.49
IMS-2	23.86	2000	2200	6700	1100	1.2	270	32.1	0.09
								23.0	0.60
IMS-3	23.77	440	540	2300	37	1.2	180	32.0	0.40
								25.3	0.39
IMS-4	23.66	2000	1800	89	1200	35	38	32.7	0.48
								27.8	0.29

EC: electrical conductivity, TDS: total dissolved solids, TSS: total suspended solids, SO_4: dissolved sulfate, Fe: iron.

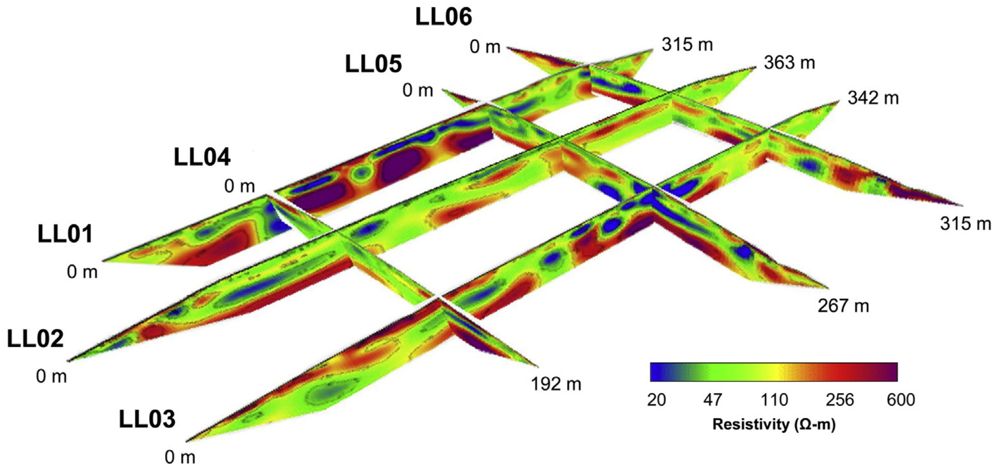

Fig. 6. Fence display of the six inverted 2D resistivity images of the Lingan WRP.

correlating to the general extent of the waste rock, and (iii) a discontinuous, high resistivity layer towards the base of each cross-section.

Fig. 7 presents the inverted resistivity images for the longitudinal lines LL01, LL02 and LL03. Geological information obtained from historical boreholes and test pits has been added to each image to both confirm and assist the electro-stratigraphic interpretation. The black dashed line in each image is the estimated bedrock elevation inferred from the geological logs, with linear interpolation between each log location.

In all images, the near-surface layer along the plateau sections of the WRP were only moderately resistive (~70 Ω-m), which was expected as this region includes the cover material that can store high levels of moisture. In contrast, near-surface material along the sloped sections were more resistive (>150 Ω-m), which corresponds to increased surface water run-off and lower moisture contents. This spatial variation in near-surface moisture content is confirmed by installed time-domain reflectometry (TDR) moisture sensors.

The next layer below the cover is characterized by high heterogeneity and moderately low resistivity, with a significant volume ranging between 5 Ω-m and 80 Ω-m. The thickness of this layer is approximately 15 m to 20 m. This low resistivity can be explained by the large amounts of dispersed sulfide minerals, acidic leachates and clay-sized particles that can exist in waste rock (e.g., Anterrieu et al., 2010; Mele et al., 2013). Some of the least resistive regions are located towards the bottom of the waste material, which likely corresponds to the increasing water saturation with depth and also the accumulation of AMD-impacted pore-water seeping downward towards the base of the waste rock. For example, these regions of low resistivity are evident at

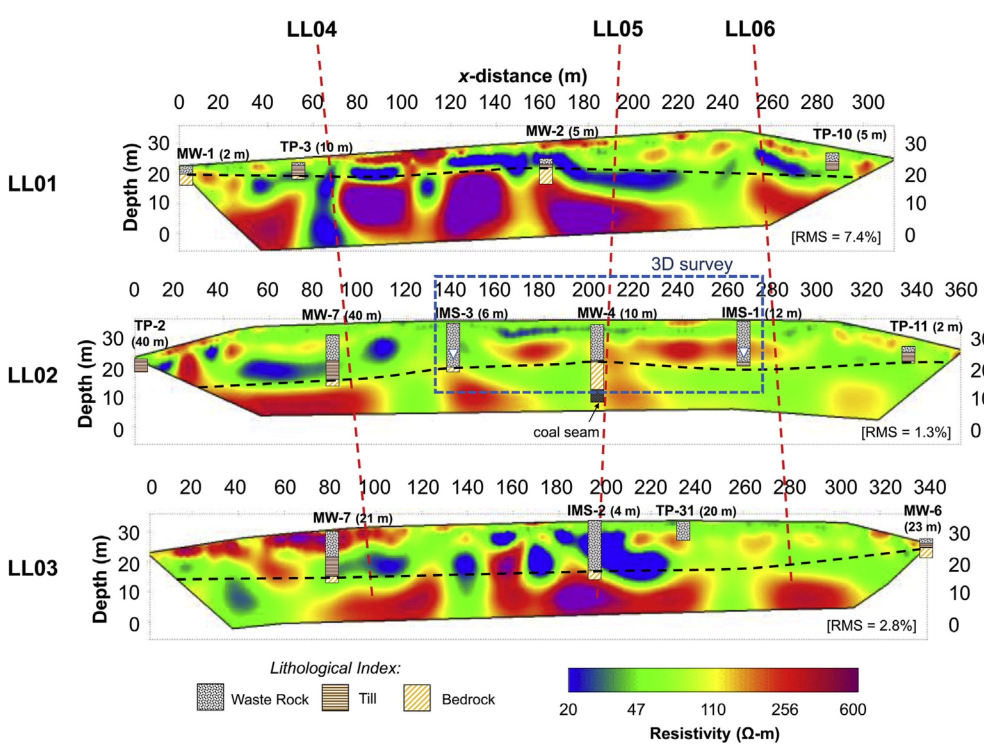

Fig. 7. Inverted DC resistivity images of lines LL01, LL02, and LL03. Available geological logs are included along with a lithological index. The offset distance from the survey line to the geological log location is shown in parentheses. The horizontal black dashed line is the bedrock elevation estimated from the geological logs (linear interpolation between each log). The red dashed lines indicate the location of the intersecting lines LL04, LL05 and LL06.

traverse distances of 80 m and 140 m along LL01, 60 m along LL02, and 100 m and 200 m along LL03. IMS-3 is located at 140 m along LL02 and the associated electrical depth profile in Fig. 5 indicates a relatively low and homogeneous resistivity with depth at this location, which correlates to the resistivity image in Fig. 7. Similarly, IMS-2 is located at 200 m along LL03 and its electrical profile in Fig. 5 confirms the very low and homogenous resistivity shown in Fig. 7.

One of the few areas where low resistivities do not exist is between 200 m and 280 m along LL02. IMS-1 is located at 265 m along LL02 and its electrical depth profile (Fig. 5) also indicates an increase in resistivity below an elevation of 31 masl. This zone may have a lower concentration of AMD-generating minerals and the complementary IP results may be able to provide a better explanation. The entire southern slope of LL03 (<100 m) exhibits high resistivity which may be caused by the typical WRP construction process of 'end dumping' close to the external slopes of the pile (e.g., Anterrieu et al., 2010). As a result, inadequate compaction may have occurred along the slopes which, in addition to coarse-grained materials and increased drainage and run-off, may be causing the observed high resistivities.

Underlying the waste material is a discontinuous, highly resistive layer which is indicative of a bedrock unit containing fractures. For instance, distinct fractures are evident at 65 m and 240 m along LL01, 120 m and 190 m along LL02, and 140 m and 250 m along LL03. Based on prior knowledge of geology at the site and the lithological descriptions in geological logs, the bedrock is generally characterized as soft, brown/grey highly fractured and highly weathered sandstone. This indicates that numerous fractures are possible and would correspond to the resistivity interpretation. The amount and location of these fractures is highly relevant as they can provide preferential flow pathways for AMD-contaminated water to migrate to larger depths.

The geological logs confirm the electro-stratigraphic interpretation of LL01 to LL03. For instance, the elevation at the top of the bedrock at MW-2, located at 160 m along LL01, corresponds to the top of the high resistivity layer. This correlation is also evident at MW-7 and IMS-3 in LL02 and IMS-2 in LL03. It should be noted that the black dashed line is estimated from sparsely located geological logs and indicates a continuous bedrock unit with no fractures. This highlights the value of continuous resistivity imaging to reveal a discontinuous bedrock that likely contains fractures.

Fig. 8 presents the inverted resistivity images for the 'perpendicular' lines LL04, LL05 and LL06. Again, geological information has been added along with a black dashed line that represents the estimated top elevation of the bedrock. The images identify the same key structural features displayed in Fig. 7: (i) near-surface material exhibits low resistivity on the plateau but high resistivity on the slopes, (ii) moderately low resistivity and highly heterogeneous waste material layer with regions of low resistivity near the base, and (iii) discontinuous and highly resistive layer indicative of fractured bedrock.

The electrical depth profiles for IMS-1, IMS-2 and IMS-4 can be used to assist the interpretation of the waste material in Fig. 8. The increase of resistivity at 150 m along LL06 was confirmed by the IMS-1 electrical depth profile in Fig. 5, where an increase in resistivity was observed below 30 masl. Similarly, the homogeneous and low resistivity in the waste material at 70 m and 170 m along LL05 is confirmed by the electrical depth profiles of IMS-4 and IMS-2, respectively.

LL04, LL05 and LL06 lines are orientated parallel to the southeast-to-northwest groundwater flow direction beneath the WRP (Fig. 2b). Therefore, in Fig. 8, groundwater is flowing from right-to-left in each resistivity image. This preferential flow of AMD water is indicated by the low resistivity bodies on the left-hand side of each image, which

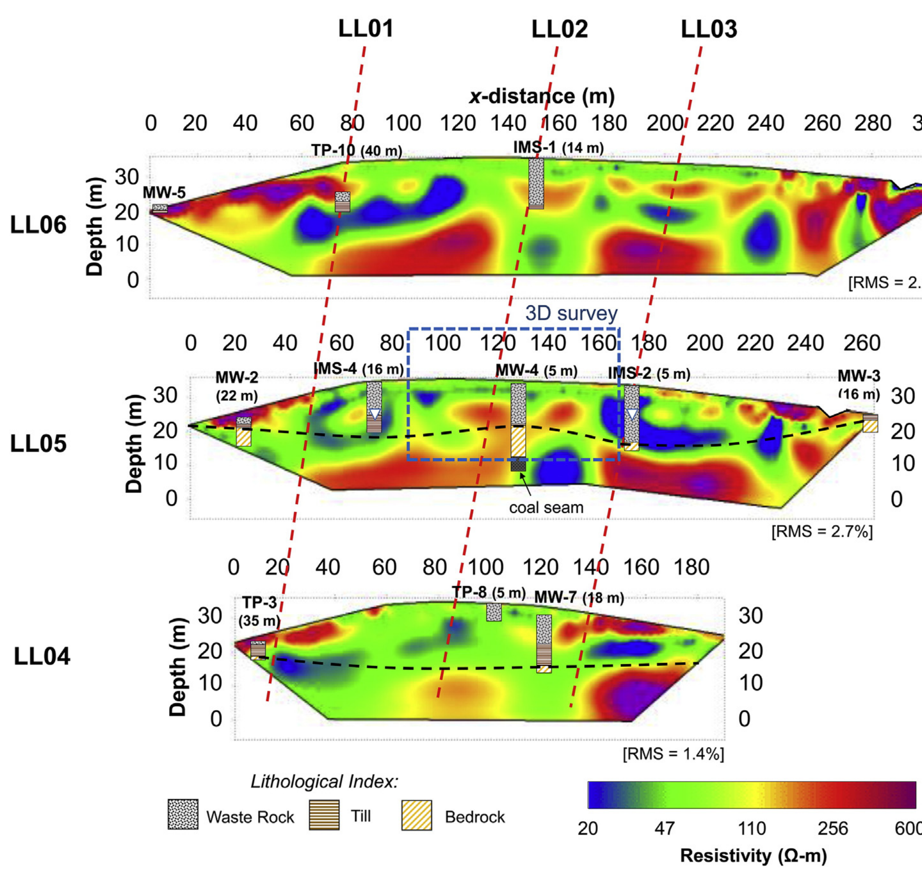

Fig. 8. DC resistivity images of lines LL06, LL05, and LL04. Available geological logs are included along with a lithological index. The red dashed lines indicate the location of the intersecting lines LL01, LL02 and LL03.

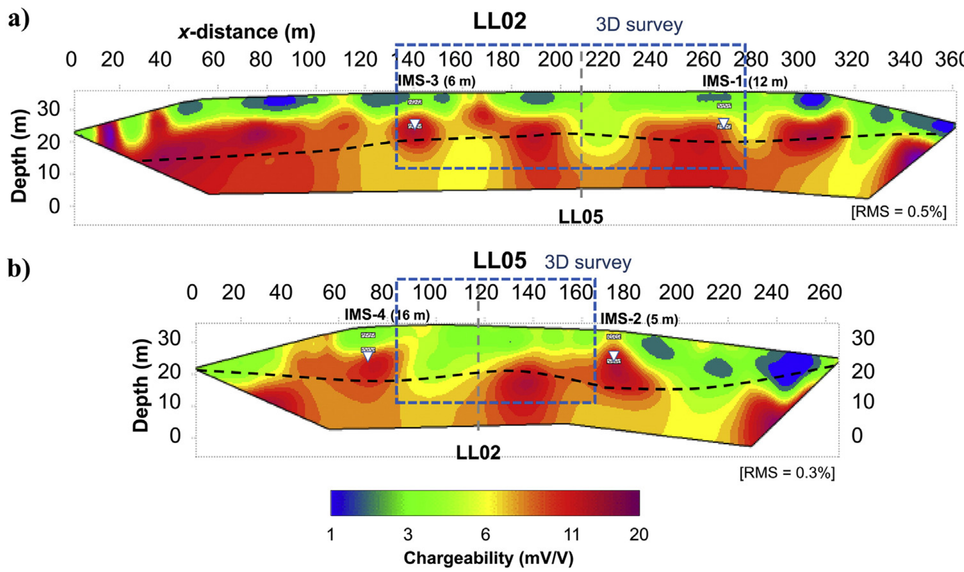

Fig. 9. Inverted chargeability images of (a) LL02, and (b) LL05 survey lines. Available geological logs with ABA analysis are indicated.

possibly indicates acidic leachate seeping downwards from the waste rock and then flowing to the left. This is in strong contrast to the highly resistive zones on the right-hand side, particularly in LL05 and LL06, which were extended outside the WRP landform to upgradient 'clean' bedrock. A specific feature of interest is the large low resistivity body located at 170 m along LL05, near the intersection with LL03. This feature is also evident at 190 m along LL03. Furthermore, IMS-2 was installed at this location, with the associated resistivity depth profile (Fig. 5) confirming a low resistivity region through the full depth of the waste material.

There are two bedrock features of interest in the resistivity images that can be validated by geological logs. First, the very low resistivity body within the bedrock at 140 m along LL05 may be explained by MW-4 where a 'coal seam' was logged at a similar elevation. Second, the inferred fracture in the bedrock at 120 m along LL04 coincides with MW-7. The geological log indicated bedrock at the base of MW-7 which was described as 'very poor to poor grey sandstone with some soil infilling between fractures'. This suggests fractures exist at this location and provide confidence in the imaged bedrock discontinuities.

3.2.2. Chargeability

Fig. 9 presents the inverted chargeability images from LL02 and LL05. The locations of known sulfide concentrations are included along with a dashed black line to indicate the estimated bedrock elevation. It is evident in both lines that the uppermost part of the waste material has low chargeability, with regions of highest chargeability (>13 mV/V) located within the bottom half of the waste rock. The highest chargeability zones generally correspond to the low resistivity zones in Figs. 7 and 8. For instance, the high chargeability zone between 40 m and 90 m along LL02 corresponds to the low resistivity zone in Fig. 7. Similarly, the high chargeability zones at 140 m and 180 m along LL05 correlate to low resistivity zones in Fig. 8.

The magnitude of the chargeability values in LL02 and LL05 reveal that the waste material does not contain significant quantities of reactive minerals, which was already confirmed by ABA tests. Nevertheless, the chargeability values are still in line with those observed in numerous studies of waste materials (e.g., Dahlin, 2001; Slater and Lesmes, 2002). Campbell et al. (1998) obtained similar IP responses at a WRP with a similar sulfide concentration (<1 wt%).

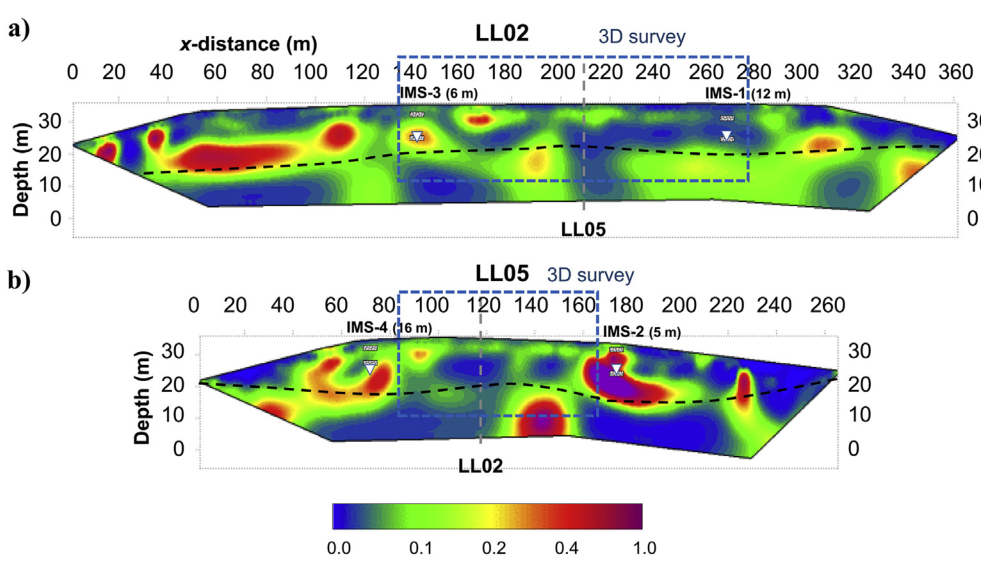

Fig. 10. Normalized chargeability images of (a) LL02, and (b) LL05 survey lines. Available geological logs with ABA analysis are indicated.

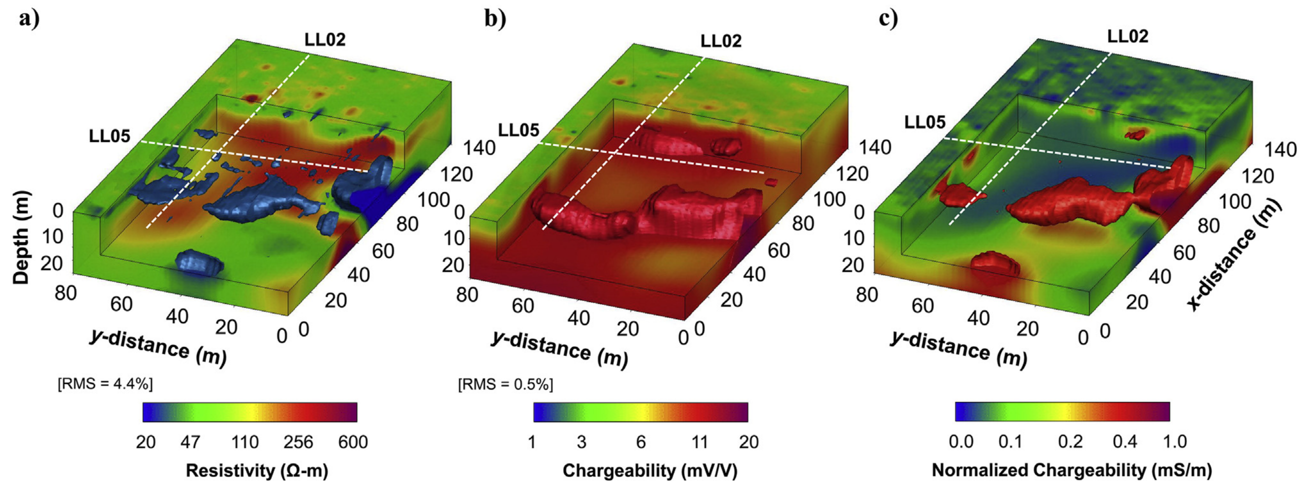

Fig. 11. 3D inverted images of (a) resistivity, (b) chargeability, and (c) normalized chargeability. In each image, the domain is partially cut-away to visualize internal variation and a selected isosurface. The isosurface values for resistivity, chargeability and normalized chargeability are 30 Ω-m, 13 mV/V and 0.4 mS/m, respectively.

3.2.3. Normalized chargeability

It is difficult to distinguish between the polarization effects due to pore-water salinity and lithology. As a result, the normalized chargeability was used to better delineate the IP response generated by mineralogy only. Fig. 10 presents the normalized chargeability images for LL02 and LL05. It is evident that almost all chargeable zones are located above the bedrock and within the lower elevations of the waste material. The only region where a high normalized chargeability is evident within the bedrock is at 140 m along LL05. As discussed earlier, this location coincides with a coal seam that may be causing this high IP response.

Figs. 8 to 10 confirm that most locations with high chargeability also exhibited low resistivity, which typically represents reactive minerals (e.g., concentrations of sulfide minerals). Locations that exhibit low resistivity and low chargeability (e.g., 230 m along LL05) may represent sulfate, an indicator of generated AMD.

3.3. 3D imaging of waste rock composition

The 2D resistivity, chargeability and normalized chargeability images have demonstrated the general structure and volume of the waste rock, highlighting low resistivity regions that may correspond to acid leachate, and chargeable regions that may correspond to concentrations of sulfide minerals. However, these individual survey lines were sparsely located with large offsets (>70 m) and full continuous 3D imaging is necessary to further analyze the compositional features of interest in the waste rock.

Fig. 11 presents the 3D domains for resistivity, chargeability and normalized chargeability. Each domain is partially cutaway to permit internal visualization. The 2D survey lines that intersect the 3D domain somewhat centrally in both orientations, LL02 and LL05, are indicated by the white dashed lines. Similarly, the intersection of the 3D domain with LL02 and LL05 is indicated by the blue dashed box in Figs. 7, 8 and 9.

Fig. 11a presents the 3D resistivity distribution. Since the 3D survey was conducted only on the plateau of the WRP, the near-surface material exhibited relatively high moisture levels which are evident by the relatively low resistivities along the surface. The cutaway depth corresponds with the approximate thickness of the waste material so the high resistivity layer at the base of the cutaway roughly coincides with the top of the bedrock. The blue isosurface of the lowest resistivities (<30 Ω-m) is attributed to highly conductive leachate zones (i.e., generated AMD), corresponding with the low resistivity regions shown in LL02 and LL05. For example, the very low resistivity body at y-distance = 0 m and x-distance = 80 m in Fig. 11a is the same body at 170 m in LL05 (Fig. 8).

Fig. 11b presents the 3D chargeability distribution. Again, this corresponds with the general structure indicated by the 2D images in Fig. 9 with the highest chargeabilities near the base of the waste material. The red isosurface represents zones of highest chargeability (>13 mV/V), which are due to both pore-water salinity and waste mineralogy. The location of the isosurface is generally similar to that of the low resistivity isosurface.

The normalized chargeability in Fig. 11c better delineates the IP response generated by mineralogy only. It is evident that almost all IP responses are located above the bedrock and within the lower elevations of the waste material. The red isosurface represents zones of highest normalized chargeability (>0.4 mS/m) which are interpreted as zones containing the highest concentrations of sulfide minerals.

Fig. 12. Aerial view of the Lingan WRP and superimposed regions of high normalized chargeability zones that likely contain the highest concentrations of sulfide minerals. The white dashed box is the outline of the 3D DC-IP survey.

3.4. Reactive mineral zones in WRP

Information on the location of acid leachate and high concentrations of sulfide minerals is extremely valuable to highlight the zone where AMD generation and release are likely to occur. Fig. 12 superimposes the location of zones of highest normalized chargeability over the landform of the WRP. As shown, these inferred high concentrations of sulfide minerals exist between IMS-2, IMS-3 and IMS-4. This suggests that the southwestern portion of the WRP is potentially more reactive and producing more AMD. This increase of AMD corresponds to the low resistivities that have also been observed in this portion of the WRP.

4. Conclusions

A geoelectrical study, combining DC resistivity and IP (DC-IP), was performed to characterize the internal composition of a WRP at the former Lingan Mine Colliery in Nova Scotia, Canada. 2D DC-IP imaging extending across the full WRP landform was first performed to assess the general structure and heterogeneity within the waste rock and hosting bedrock. The DC-IP profiles indicated a highly heterogeneous and moderately conductive waste material overlying a bedrock unit comprising several fractures. Very low resistivity regions were interpreted as acid leachate, with coincident regions exhibiting high chargeability and high normalized chargeability. These were interpreted as reactive minerals, likely to be sulfides. Integration of geological and geochemical information assisted and confirmed this interpretation. 3D DC-IP imaging was next performed to specifically focus on the composition of the waste material at the centre of the WRP. Continuous 3D isosurfaces of low resistivity ($<30\ \Omega$-m) and high normalized chargeability (>0.4 mS/m) were interpreted as regions of generated AMD (acid leachate) and stored (yet to be generated) AMD (sulfide minerals).

Although this study highlighted the potential of DC-IP for WRP studies, it is acknowledged that some limitations exist. The highly heterogeneous chemical and physical features typically found in waste rock, such as porosity, moisture content and mineralogical composition, make interpretation very difficult. So while the integration of geological and/or geochemical information into any geoelectrical study is encouraged, it is particularly welcome in WRP studies. In this study, standalone electro-stratigraphic interpretation was possible but the inclusion of known geological and geochemical information assisted and increased confidence in the interpretation. For instance, the geoelectrically inferred bedrock was confirmed at several locations by the geological logs. This then provided confidence in the inferred bedrock fractures located between the log locations. It should also be noted that the time needed for IP data acquisition is considerably longer than DC data acquisition, which is a factor to consider for long survey line lengths that may be encountered at WRPs. In this study, 2.5 m and 3 m electrode spacings were used to optimize survey time; however, the smaller heterogeneities such as fine-grained, meter-scaled layers (e.g., thin till layer below the waste rock), were not resolved. Furthermore, WRPs can contain relatively low concentrations of sulfide minerals (<1 wt%) and make IP detection difficult; therefore, the acquisition of high quality IP data, as shown in this study, may be necessary to ensure locations with low reactivity are delineated.

The application of combined DC-IP is highly promising for WRP characterization. The two datasets are highly complementary for WRP investigations due to the expected overlapping properties of interest: a conductive leachate co-existing with reactive mineralogy. Knowledge on where a WRP contains higher stored and/or generated AMD is extremely valuable and can help optimize remedial design and monitoring programs. New structural information obtained from a DC-IP study can help to refine conceptual and quantitative models of AMD processes and improve the design and long-term performance of remedial strategies.

Acknowledgements

This work was conducted under the CAPs Monitoring Project and funded by Enterprise Cape Breton Corporation (ECBC) which was later dissolved into Public Works and Government Services Canada (PWGSC). The authors wish to thank the anonymous reviewers for their constructive comments for the improvement of this manuscript. The authors would like to give special thanks to Joseph MacPhee and Joseph Shea (PWGSC) for their support during this study. The authors would also like to thank David Mayich (Mayich Consulting) for sharing his expertise on the site and Dr. George Vargemezis (Aristotle University of Thessaloniki, Greece) for helping to produce the resistivity fence diagram.

References

Amos, R.T., Blowes, D.W., Bailey, B.L., Sego, D.C., Smith, L., Ritchie, A.I.M., 2015. Waste-rock hydrogeology and geochemistry. Appl. Geochem. 57:140–156. https://doi.org/10.1016/j.apgeochem.2014.06.020.

Anterrieu, O., Chouteau, M., Aubertin, M., 2010. Geophysical characterization of the large-scale internal structure of a waste rock pile from a hard rock mine. Bull. Eng. Geol. Environ. 69:533–548. https://doi.org/10.1007/s10064-010-0264-4.

Aristodemou, E., Thomas-Betts, A., 2000. DC resistivity and induced polarization investigations at a waste disposal site and its environments. J. Appl. Geophys. 44:275–302. https://doi.org/10.1016/S0926-9851(99)00022-1.

Binley, A., Hubbard, S.S., Huisman, J.A., Revil, A., Robinson, D.A., Singha, K., Slater, L.D., 2015. The emergence of hydrogeophysics for improved understanding of subsurface processes over multiple scales. Water Resour. Res. 51 (6):3837–3866. https://doi.org/10.1002/2015WR017016.

Buselli, G., Hwang, H.S., Lu, K., 1998. Minesite groundwater contamination mapping. Explor. Geophys. 29 (3–4):296–300. https://doi.org/10.1071/EG998296.

Campbell, D.L., Fitterman, D.V., 2000. Geoelectrical methods for investigating mine dumps. ICARD 2000 — Proceedings from the Fifth International Conference on Acid Rock Drainage:pp. 1513–1523 https://doi.org/10.4133/1.2922567.

Campbell, D.L., Fitterman, D.V., Hein, A.S., Jones, D.P., 1998. Spectral induced polarization studies of mine dumps near Silverton, Colorado. Proceedings of the Symposium on the Application of Geophysics to Engineering and Environmental Problems (SAGEEP), March 22–26, 1998, Chicago, Illinois, pp. 761–769.

Campos, D., Chouteau, M., Aubertin, M., 2003. Using geophysical methods to image the internal structure ofminewaste rock piles. 9th European Meeting of Environmental and Engineering Geophysics, Paper O-008, Prague, Czech Republic, Aug. 31–Sep. 4, 2003.

Carlson, N., Bouzid, N., Byrd, R., 2015. Environmental applications of the IP method: surveys of subsurface waste. Lead. Edge 34 (2):214–220. https://doi.org/10.1190/tle34020214.1.

Chambers, J.E., Kuras, O., Meldrum, P.I., Ogilvy, R.D., Hollands, J., 2006. Electrical resistivity tomography applied to geologic, hydrogeologic, and engineering investigations at a former waste-disposal site. Geophysics 71 (6):B231–B239. https://doi.org/10.1190/1.2360184.

Dahlin, T., 2001. The development of DC resistivity imaging techniques. Comput. Geosci. 27 (9):1019–1029. https://doi.org/10.1016/S0098-3004(00)00160-6.

Dahlin, T., Zhou, B., 2006. Multiple gradient array measurements for multi-channel 2D resistivity imaging. Near Surface Geophysics 4 (2), 113–123.

van Dam, R., Gutierrez, L., McLemore, V., Wilson, G.W., Hendrickx, J., Walker, B., 2005. Near surface geophysics for the structural analysis of a mine rock pile, Northern NewMexico. Paper Presented at the 2005 National Meeting of the American Society of Mining and Reclamation, June 19–23, 2005. published by ASMR, 3134 Montavesta Rd., Lexington, KY 40502.

Doetsch, J., Fiandaca, G., Auken, E., Christiansen, A.V., Cahill, A.G., 2015. Field-scale time-domain spectral induced polarization monitoring of geochemical changes induced by injected CO_2 in a shallow aquifer. Geophysics 80 (2):WA113–WA126. https://doi.org/10.1190/geo2014-0315.1.

Fala, O., Molson, J.W., Aubertin, M., Bussière, B., 2005. Numerical modelling of flow and capillary barrier effects in unsaturated waste rock piles. Mine Water Environ. 24 (4):172–185. https://doi.org/10.1007/s10230-005-0093-z.

de Franco, R., Biella, G., Tosi, L., Teatini, P., Lozej, A., Chiozzotto, B., Giada, M., Rizzetto, F., Claude, C., Mayer, A., Bassan, V., Gasparetto-Stori, G., 2009. Monitoring the saltwater intrusion by time lapse electrical resistivity tomography: the Chioggia test site (Venice Lagoon, Italy). J. Appl. Geophys. 3–4:117–130. https://doi.org/10.1016/j.jappgeo.2009.08.004.

Gazoty, A., Fiandaca, G., Pedersen, J., Auken, E., Christiansen, A.V., 2012. Mapping of landfills using time-domain spectral induced polarization data: the Eskelund case study. Near Surface Geophysics 10 (6):575–586. https://doi.org/10.3997/1873-0604.2012046.

Gonzales Amaya, A., Dahlin, T., Barmen, G., Rosberg, J.-E., 2016. Electrical resistivity tomography and induced polarization for mapping the subsurface of alluvial fans: a case study in Punata (Bolivia). Geosciences 6 (4):51. https://doi.org/10.3390/geosciences6040051.

INAP (The International Network for Acid Prevention), 2014. Global Acid Rock Drainage Guide. http://gardguide.com/images/5/5f/TheGlobalAcidRockDrainageGuide.pdf, Accessed date: 28 August 2017.

Johansson, S., Fiandaca, G., Dahlin, T., 2015. Influence of non-aqueous phase liquid configuration on induced polarization parameters: conceptual models applied to a time-domain field case study. J. Appl. Geophys. 123:295–309. https://doi.org/10.1016/j.jappgeo.2015.08.010.

Kim, J.H., 2016. DC_2DPro: User's Manual. Geoelectric Imaging Laboratory: Korea Institute of Geoscience and Mineral Resources, Daejeon, South Korea.

Kim, J.H., Supper, R., Ottowitz, D., Jochum, B., Yi, M.J., 2016. Processing of ERT monitoring data and evaluation of their reliabilities. Near Surface Geoscience 2016 - 22nd European Meeting of Environmental and Engineering Geophysics. 4–8 September 2016, Barcelona, Spain https://doi.org/10.3997/2214-4609.201602020.

Ladwig, K.J., 1983. Electromagnetic induction methods for monitoring acid mine drainage. Groundwater Monitoring and Remediation 3 (1):46–51. https://doi.org/10.1111/j.1745-6592.1983.tb00857.x.

Loke, M.H., 2016. Tutorial: 2-D and 3-D Electrical Imaging Surveys. http://www.geotomosoft.com/downloads.php, Accessed date: 15 June 2017.

Loke, M.H., Chambers, J.E., Rucker, D.F., Kuras, O., Wilkinson, P.B., 2013. Recent developments in the direct-current geoelectrical imaging method. J. Appl. Geophys. 95: 135–156. https://doi.org/10.1016/j.jappgeo.2013.02.017.

Mele, M., Servida, D., Lupis, D., 2013. Characterisation of sulphide-bearing waste-rock dumps using electrical resistivity imaging: the case study of the Rio Marina mining district (Elba Island, Italy). Environ. Monit. Assess. 185 (7):5891–5907. https://doi.org/10.1007/s10661-012-2993-2.

Nivorlis, A., 2017. Processing and Modeling of Induced Polarization Data. Masters Thesis. Aristotle University of Thessaloniki, Thessaloniki, Greece (January 2017).

Nivorlis, A., Tsourlos, P., Vargemezis, G., Tsokas, G., Kim, J.H., Yi, M.J., 2017. Processing and modeling of time domain induced polarization data. Near Surface Geoscience 2017 – 23rd European Meeting of Environmental and Engineering Geophysics. 3–7 September 2017, Malmo, Sweden https://doi.org/10.3997/2214-4609.201702085.

Nordstrom, D.K., Blowes, D.W., Ptacek, C.J., 2015. Hydrogeochemistry and microbiology or mine drainage: an update. Appl. Geochem. 57:3–16. https://doi.org/10.1016/j.apgeochem.2015.02.008.

Olsson, P.I., Dahlin, T., Fiandaca, G., Auken, E., 2015. Measuring time-domain spectral induced polarization in the on-time: decreasing acquisition time and increasing signal-to-noise ratio. J. Appl. Geophys. 123:316–321. https://doi.org/10.1016/j.jappgeo.2015.08.009.

Papadopoulos, N.G., Tsourlos, P., Tsokas, G.N., Sarris, A., 2006. Two-dimensional and three-dimensional resistivity imaging in archaeological site investigation. Archaeol. Prospect. 13:163–181. https://doi.org/10.1002/arp.276.

Poisson, J., Choteau, M., Aubertin, M., Campos, A., 2009. Geophysical experiments to image the shallow internal structure and the moisture distribution of a mine waste rock pile. J. Appl. Geophys. 67:179–192. https://doi.org/10.1016/j.jappgeo.2008.10.011.

Power, C., Gerhard, J.I., Tsourlos, P., Giannopoulos, A., 2013. A new coupled model for simulating the mapping of dense nonaqueous phase liquids using electrical resistivity tomography. Geophysics 78 (4):EN1–EN15. https://doi.org/10.1190/geo2012-0395.1.

Power, C., Ramasamy, M., Mkandawire, M., MacAskill, D., MacPhee, J., Shea, J., Mayich, D., Baechler, F., 2017a. Five-year performance monitoring of a high-density polyethylene (HDPE) cover system at a reclaimed mine waste rock pile in the Sydney Coalfield (Nova Scotia, Canada). Environ. Sci. Pollut. Res. 24 (34), 26744–26762.

Power, C., Tsourlos, P., Gerhard, J.I., Dahlin, T., 2017b. Simulated time-lapse DC-IP monitoring of dense non-aqueous phase liquids (DNAPLs) – an initial approach. Near Surface Geoscience 2017 – 23rd European Meeting of Environmental and Engineering Geophysics. 3–7 September 2017, Malmo, Sweden https://doi.org/10.3997/2214-4609.201702030.

Revil, A., Karaoulis, M., Johnson, T., Kemna, A., 2012. Review: some low-frequency electrical methods for subsurface characterization and monitoring in hydrogeology. Hydrogeol. J. 20:617–658. https://doi.org/10.1007/s10040-011-0819-x.

Rucker, D.F., Glaser, D.R., Osborne, T., Maehl, W.C., 2009. Electrical resistivity characterization of a reclaimed gold mine to delineate acid rock drainage pathways. Mine Water Environ. 28 (2):146–157. https://doi.org/10.1007/s10230-009-0072-x.

Slater, L., Lesmes, D., 2002. IP interpretation in environmental investigations. Geophysics 67 (1):77–88. https://doi.org/10.1190/1.1451353.

Slater, L.D., Ntarlagiannis, D., Day-Lewis, F.D., Mwakanyamale, K., Versteeg, R.J., Ward, A., Strickland, C., Johnson, C.D., Lane, J.W., 2010. Use of electrical imaging and distributed temperature sensing methods to characterize surface water–groundwater exchange regulating uranium transport at the Hanford 300 Area, Washington. Water Resour. Res. 46, W10533. https://doi.org/10.1029/2010WR009110.

Spindler, K., Olyphant, G., 2004. Geophysical investigations at an abandoned mine site subjected to reclamation using a fixated scrubber sludge cap. Environ. Eng. Geosci. 10 (3):243–251. https://doi.org/10.2113/10.3.243.

Yuval, Oldenburg, D.W., 1996. DC resistivity and IP methods in acid mine drainage problems: results from the Copper Cliff mine tailings impoundments. J. Appl. Geophys. 33 (4):187–198. https://doi.org/10.1016/0926-9851(95)00020-8.

Zhou, Q.Y., Shimada, J., Sato, A., 2001. Three-dimensional spatial and temporal monitoring of soil water content using electrical resistivity tomography. Water Resour. Res. 37: 273–285. https://doi.org/10.1029/2000WR900284.